Spatial coding defects of hippocampal neural ensemble calcium activities in the triple-transgenic Alzheimer's disease mouse model

Xiaoxiao Lin[a,1], **Lujia Chen**[a,f,1], **David Baglietto-Vargas**[b,c,1], **Parsa Kamalipour**[a], **Qiao Ye**[a,f], **Frank M. LaFerla**[c], **Douglas A. Nitz**[d,g], **Todd C. Holmes**[e,g], **Xiangmin Xu**[a,c,f,g,*]

[a]Department of Anatomy and Neurobiology, School of Medicine, University of California, Irvine, CA 92697, United States of America

[b]Departamento Biologia Celular, Genetica y Fisiologia, Instituto de Investigacion Biomedica de Malaga-IBIMA, Centro de Investigacion Biomedica en Red Sobre Enfermedades Neurodegenerativas (CIBERNED), Facultad de Ciencias, Universidad de Malaga, Malaga 29071, Spain

[c]Institute for Memory Impairments and Neurological Disorder, University of California, Irvine, CA 92697, United States of America

[d]Department of Cognitive Science, University of California, San Diego, CA 92093, United States of America

[e]Department of Physiology and Biophysics, School of Medicine, University of California, Irvine, CA 92697, United States of America

[f]Department of Biomedical Engineering, University of California, Irvine, CA 92697, United States of America

[g]Center for Neural Circuit Mapping, University of California, Irvine, CA 92697, United States of America

Abstract

*Corresponding author at: Department of Anatomy and Neurobiology, School of Medicine, University of California, Irvine, CA 92697-1275, United States of America. xiangmix@hs.uci.edu (X. Xu).

[1]X.L., L.C. and D.B.V. contributed equally to this work.

Alzheimer's disease (AD) causes progressive age-related defects in memory and cognitive function and has emerged as a major health and socio-economic concern in the US and worldwide. To develop effective therapeutic treatments for AD, we need to better understand the neural mechanisms by which AD causes memory loss and cognitive deficits. Here we examine large-scale hippocampal neural population calcium activities imaged at single cell resolution in a triple-transgenic Alzheimer's disease mouse model (3xTg-AD) that presents both amyloid plaque and neurofibrillary pathological features along with age-related behavioral defects. To measure encoding of environmental location in hippocampal neural ensembles in the 3xTg-AD mice in vivo, we performed GCaMP6-based calcium imaging using head-mounted, miniature fluorescent microscopes ("miniscopes") on freely moving animals. We compared hippocampal CA1 excitatory neural ensemble activities during open-field exploration and track-based route-running behaviors in age-matched AD and control mice at young (3–6.5 months old) and old (18–21 months old) ages. During open-field exploration, 3xTg-AD CA1 excitatory cells display significantly higher calcium activity rates compared with Non-Tg controls for both the young and old age groups, suggesting that in vivo enhanced neuronal calcium ensemble activity is a disease feature. CA1 neuronal populations of 3xTg-AD mice show lower spatial information scores compared with control mice. The spatial firing of CA1 neurons of old 3xTg-AD mice also displays higher sparsity and spatial coherence, indicating less place specificity for spatial representation. We find locomotor speed significantly modulates the amplitude of hippocampal neural calcium ensemble activities to a greater extent in 3xTg-AD mice during open field exploration. Our data offer new and comprehensive information about age-dependent neural circuit activity changes in this important AD mouse model and provide strong evidence that spatial coding defects in the neuronal population activities are associated with AD pathology and AD-related memory behavioral deficits.

Keywords

1. Introduction

Alzheimer's disease (AD) is an incurable age-related progressive neurodegenerative disorder. Individuals diagnosed with AD undergo a progressive loss of memory, cognition, language skills and personality traits (Alzheimer's Association, 2020; Weller and Budson, 2018). Currently, the neural mechanisms by which AD causes memory loss and cognitive deficits remain poorly understood. However, recent imaging studies from clinical and animal models imply that neuronal dysfunction and functional disruption of neuronal circuits in the brain strongly contribute to memory deficits in AD cases (Busche and Konnerth, 2016; Frere and Slutsky, 2018). As the number of AD cases steadily increase each year and current treatments are only palliative, further understanding of AD-related neural mechanisms is needed for the development of meaningful new treatment strategies for improving memory and prolonging healthy cognitive function (Bast et al., 2017; Harris et al., 2020; Selkoe, 2002).

One of the major brain areas affected in AD patients is hippocampal formation. This brain region and its connections with several cortical areas play essential roles in spatial cognition and episodic memory processes. Recent studies in humans, and supported by animal models, show that the CA1 projection to the subiculum (SUB) area is significantly affected in AD (Busche et al., 2012; Lerdkrai et al., 2018). CA1 and SUB regions project to diverse cortical areas that include the entorhinal, retrosplenial and perirhinal cortex, and these cortical areas are implicated in multiple forms of spatial cognition and memory processes (Cembrowski et al., 2018; Naber et al., 2000; Xu et al., 2016). Moreover, alterations in the balance of neural circuit excitation/inhibition have been found in AD, which may underlie dysfunctional circuit changes observed in AD cases (Busche et al., 2012). Several studies in AD animal models have shown that pathologically associated neural activity is a major feature in these models. Interestingly, neuronal hyperactivity or hypo-activity has been described in the vicinity of amyloid plaque formation (Busche et al., 2012; Grienberger et al., 2012; Palop and Mucke, 2016; Yang et al., 2018), suggesting that aberrant neuronal activity changes are associated with the defects in cognitive processes in AD brains.

Here, we used in vivo GCaMP6-based calcium imaging with head-mounted, miniature fluorescent microscopes ("miniscopes") on freely moving animals (Cai et al., 2016; Chen et al., 2013; Ziv et al., 2013(Sun et al., 2019)) to study CA1 neural circuit ensemble coding associated with AD-related memory impairments in a triple-transgenic Alzheimer's disease mouse model (3xTg-AD). Head-mounted miniscope imaging enables us to longitudinally examine hundreds of brain cells in action at single-cell resolution, as the animal freely explores environments.

The 3xTg-AD mouse model contains three mutations in homologous mouse genes associated with human familial Alzheimer's disease (APP Swedish, MAPT P301L, and PSEN1 M146V), and displays age-dependent plaque and tangle pathology. Extracellular amyloid-beta (Aβ) deposits appear by 6 months and become progressively more extensive by 12 months in 3xTg-AD mouse brains. Although tau pathology is not robustly observed in 3xTg-AD mice by six months of age, aggregates of conformationally-altered and hyperphosphorylated tau are detected in the hippocampus of 3xTg-AD mice by 12–15 months (Billings et al., 2005; Oddo et al., 2003).

The 3xTg-AD line reveals hippocampal spatial memory impairments at relatively earlier ages, even preceding plaque and tangle formation (Baglietto-Vargas et al., 2018; Oddo et al., 2003; Stimmell et al., 2019). We draw on a strong premise from the literature and our previous studies that memory-based behaviors rely on neural circuitry that is altered in aging and AD (Bast et al., 2017; Busche and Konnerth, 2016; Frere and Slutsky, 2018; Harris et al., 2020; Selkoe, 2002). Using in vivo miniscope imaging, we studied the neural calcium ensemble activities in hippocampal CA1 in freely behaving 3xTg-AD mice and non-transgenic controls (Non-Tg) at young (3–6.5 months old) and old (18–21 months old) ages. We find spatial coding defects in hippocampal neural calcium ensembles in the 3xTg-AD mouse model. This provides strong evidence that spatial encoding defects in hippocampal circuit ensemble activities are associated with AD-related memory behavioral deficits.

2. Material and Methods

2.1. Animals

All experiments were conducted according to the National Institutes of Health guidelines for animal care and use and were approved by the Institutional Animal Care and Use Committee and the Institutional Biosafety Committee of the University of California, Irvine. Recent publications have shown that the female 3xTg-AD mice display more robust and consistent pathology than the male mice due to the sex regulatory element in the promoter area of the genetic construct (including for amyloid beta and tau) (Belfiore et al., 2019; Carroll et al., 2010). Therefore, we used female non-transgenic (Non-Tg) and 3xTg-AD mice in this study. Our 3xTg-AD mice were provided by La Ferla's lab and the MODEL-AD UCI center, The generation of the 3xTg-AD mice has been described previously (Belfiore et al., 2019; Oddo et al., 2003). Briefly, the 3xTg-AD model was generated by co-microinjected two independent transgenes encoding human APPswe and the human TauP301L (both under the control of the mouse Thy1.2 regulatory element) into single-cell embryos harvested from homozygous mutant PS1M146V Knockin (PSI-KI) mice. We used the F1 mice from the cross of 129X1/SvJ (JAX reference 000691) with C57BL6 (JAX reference 000664) as non-transgenic controls. The mice had access to food and water in their home cages with lights maintained on a 12 h light/dark cycle.

2.2. Viral injections

In order to image in vivo calcium transients of hippocampal CA1 excitatory neurons, AAV1-CamKII(0.4)-GCaMP6f was stereotaxically injected into the mouse brain region. First, the animal was anesthetized under 2% isoflurane for 10 min with a 0.8 L/min oxygen flow rate using an isoflurane tabletop unit (HME109, Highland Medical Equipment). The mouse was then head secured in a rodent stereotaxic frame (Leica Angle Two™ for mouse) with continuous 1.5% isoflurane anesthesia. An incision was made to expose the skull, and a small craniotomy was performed for the viral injection. The coordinates of Bregma and Lambda were used as landmarks to determine the target brain region with the coordinates: anteroposterior (AP) −1.94 mm, mediolateral (ML) +1.40 mm; dorsoventral (DV) −1.35 mm (all values given relative to the bregma). The GCaMP-expressing virus (0.4 μl of AAV1-CaMKII (0.4)-GCaMP6f, 2×10^{11} GC/ml) was delivered into the target region at a rate of 20–30 nl/min with 10 ms pulse duration by a Picospritzer (General Valve, Hollis, NH). After injection, the glass pipette stayed in the brain for 5 min to prevent the backflow of the virus. A tissue adhesive (3 M Vetbond, St. Paul, MN) was used to close the incision. Three weeks later, the mouse was implanted with a GRIN lens for miniscope imaging.

2.3. Imaging experiment preparations

The related mouse surgery has been described in our published study (Sun et al., 2019). All the animals were implanted with a GRIN lens (Edmund Optics) for in vivo calcium imaging once they were recovered from AAV1-CaMKII-GCaMP6f injection. Following the same procedure of viral injection, animals were anesthetized under 2% isoflurane and placed in a heating pad with a set temperature at 37°C. After the application of 70% ethanol and Betadine on the shaved head, the skin tissue was opened. The connective tissue on the surface of the skull was removed by a swab and fine forceps. The muscle was dissected

from the edge of the skull by a scalpel. To enhance the stability of implantation and in vivo imaging quality, we used a bur (Meisinger, 1/4 Round Steel) to roughen the surface of the skull and implant a skull screw far away from the implantation area. Saline was used to wet the skull, which can reduce the overheating caused by the bur and clean up the skull. We marked a center point for a craniotomy on the exposed skull (AP: −2.3 mm, ML: +1.75 mm) and etched a 1-mm radius cranial window surrounding the center point, which allowed to fit in a 1.8 mm diameter GRIN lens. The GRIN lens was implanted in the right hemisphere because the right side of the brain tends to process spatial information while the left side of the brain relates to species-specific communication (Shinohara et al., 2012). The skull fragment was carefully removed with fine forceps and the exposed tissue was gently aspirated with a 27G flat needle. We then switched to a 29G flat needle until seeing the white striated tissue (corpus callosum) above CA1. We stopped the aspiration when the hippocampus was exposed. We then attached the prepared lens holder to the stereotaxic apparatus and gently lowered the GRIN lens to the target depth (DV: −1.55 mm). A small amount of Krazy glue was quickly applied to nearby the GRIN lens. A thick layer of dental cement (Lang Dental Manufacturing: 1304CLR) was used to secure the implant to the skull. We applied Kwik-Sil on the top of the lens to protect the lens from physical damage until the dental cement was dried. We wait for 2–3weeks for the hippocampal tissue to recover from the surgery. A miniature fluorescent microscope (miniscope) (www.miniscope.org/) was used to check neural calcium signals through a GRIN lens and to prepare for the placement of the baseplate. The baseplate was stabilized by dental cement. We then attached a cap on the baseplate to prevent the damage of the lens.

During the recording session, a light-weight miniscope (~ 3 g) was secured on the baseplate with a set screw and connected to a custom open-source data acquisition (DAQ) box through a flexible coaxial cable. The DAQ box was connected with a PC USB port for miniscope power supply and data acquisition. The DAQ and graphic user interface was written in C++ and uses Open Computer Vision libraries for image acquisition. The miniscope recording parameters was adjusted by a custom-programmed user interface. The imaging field of view is 700μm × 450μm (~0.9μm per pixel) and the image signals were acquired at ~30 frames per second and saved as uncompressed .avi files. A high resolution webcam (Logitech) was controlled simultaneously with the miniscope to record animal behavior at ~30 frames per second. The webcam and miniscope videos streams were encoded with time stamping to allow for temporal registration.

2.4. Histology and immunochemical staining

All animals were perfused after behavioral and imaging studies. 5 ml of phosphate-buffered saline (PBS) were used to push out blood in the brain and followed by 25 ml PBS containing 4% paraformaldehyde. The perfused mouse brain was soaked in 4% paraformaldehyde overnight and was switched into 30% sucrose in 1 X PBS until the brain sank. In the next, the brain was frozen in dry ice and coronally sectioned in 30 μm thickness on a microtome (Leica SM2010R, Germany). Half of the hippocampal sections were mounted for the checking of GRIN lens implantation. The contralateral hippocampal sections without the removal of cortex were immunostained with antibodies to identify the pathology of Alzheimer's Disease. To investigate the intracellular Aβ accumulation and APP-related

products, we stained hippocampal sections with mouse anti-β-Amyloid primary antibody (6E10, BioLegend, 1:500 dilution, Cat: 803010) and following by an Alexa Fluor 549 conjugated donkey anti-mouse secondary antibody (Jackson Immuno Research, 1:200 dilution). For tau staining, a mouse anti-AT8 tau antibody (Thermo Fisher, 1:250 dilution, Cat: MN1020) was used and followed by the AF549 donkey anti-mouse secondary antibody. Sections were stained with DAPI and coverslipped for imaging.

The images of immunostained sections were acquired by a fluorescent BX61 Olympus microscope. In addition, AAV-GCaMP6f expressing hippocampal sections were imaged with a confocal microscope (FV3000, Olympus) under a 20× objective lens for fluorescence intensity analysis. The acquired images were exported using the software analysis tools. The integrated fluorescence intensity of the section image was measured using Adobe Photoshop.

2.5. Behavioral experiments

All the animals were handled and habituated with a head-mounted miniscope 5 min per day for at least one week before behavioral experiments. Water restriction was used to motivate animals to move on the track and the reduction of body weights was controlled within 15%.

2.5.1. Open arenas (circle and square box)—After being well handled, animals were habituated in two open-field arenas with a head-mounted miniscope for 4 consecutive days. The circle box (36 cm in diameter) and square box (26 cm × 26 cm) were adorned with various visual cues. On the first day, animals explored the circular environment for 10 min, then were transferred to the adjacent square box for another 10 min. On the second day, animals explored in each arena for 10 min as day one except exposing to the square arena first then to the circular box. Following the habituation in two boxes on four consecutive days, animals' behavioral trajectories and neuronal activities were recorded by miniscope imaging for another four days.

2.5.2. Linear track—Mice were trained to run on the linear track for four days during the training session. The one-meter linear track is made of black plastic materials. Two water reward zones were located at the end of the linear track. The walls of reward zones were adorned with various visual cues. 10% ethanol was used to get rid of the odor cues left from other mice in the previous behavioral session. At the beginning of each session, a mouse was released in the middle of the track and ran to the end of the track to get a 10 μl of water reward. Once the mouse reached 50 laps within 10 min in a training session, we stopped and resumed experimental recording the next day. On the first day of the miniscope recording, animals were required to complete two sessions on the same track with a horizontal direction. Each mouse had a two-minute break time in the home cage between sessions. At least 40 laps per session were acquired for the data processing. On day 2, the mouse ran on the same linear track with a horizontal direction as day 1 in session 1. Then, the linear track was rotated in a 90-degree direction, named "vertical" relative to the recording environment. After 2 min of rest in the home cage, the animal went through another 40 laps on the vertical track. On the third day, the animal ran on the vertical track in session 1 then back to the horizontal track in session 2.

2.6. Data preprocessing

The raw calcium recordings were down-sampled to 15 frames/s. Motion correction was applied to the neuron recordings with the well-established motion correction streamline NormCorre (Pnevmatikakis and Giovannucci, 2017), to fix the rigid movements caused by potential scope shifts across time.

2.6.1. Extract neural calcium signal using CNMF-E method—The calcium
signal of each neuron was gathered from video data using the Extended Constrained Nonnegative Matrix Factorization (CNMF-E) framework proposed by Zhou et al. (2018b). This framework uses the following model to represent the video data:

$$y(x, t) = \sum_{i=1}^{K} a_i(x)*c_i(t) + b(x, t)$$

where $y(x,t)$ represents the raw video data, $a_i(x)$ represents the neuron's spatial footprint, $c_i(t)$ represents the calcium activity and $b(x,t)$ represents the background activity. By applying sophisticated background approximation, CNMF-E can efficiently remove baseline noise, and achieve the neuron footprint and calcium response via deconvolution. To remove false positive detections, a 2D Gaussian kernel was fit for the spatial footprint of each neuron, and Kullback–Leibler divergence was calculated between the footprint and Gaussian kernel. Kullback–Leibler divergence quantifies the similarity between two distributions, and here it represents the closeness between the actual neuron footprint and the theoretically perfect footprint. Neurons with divergence values larger than 0.6 were kept for subsequent analyses.

CNMF-E was applied to different trials independently. To identify common neurons across the trials, for each pair of extracted neurons across two trials, we calculated the level of footprint overlap between the two neurons, and the similarity of distance pattern between each neuron and its neighbors. Both measures were converted to probability values indicating the chance for the two neurons to be aligned, and the final alignment probability was the average of the overlap probability and distance pattern probability. The neuron pairs with the highest alignment probability go beyond 0.25 were considered as the same neuron across two trials.

2.6.2. Mouse movement behavior extraction—The movement trajectory was
extracted from the behavioral tracking videos simultaneously recorded with neuronal responses, at a sample rate of ~30 Hz. The bottom of the box was selected as the region of interest (ROI), to restrict the area for behavioral detection. The trajectory was defined as the positions of the red miniscope LED centroid across all frames and was smoothed using the moving average method.

2.6.3. Spatial rate map calculation—The calcium transient trains were calculated by
applying the CNMF-E embedded deconvolution algorithm, OASIS (Friedrich et al., 2017), to the extracted temporal calcium dynamics. A threshold of 10% of maximum amplitudes of the neurons' calcium transients was set for each neuron, and potential events with an amplitude lower than the threshold were excluded.

The movement trajectories were aligned with the calcium responses according to the timestamp that records the correspondence between behavioral recordings and calcium recordings. The ROI was divided into 10 mm × 10 mm bins. The total time mouse spent inside a bin was counted as the bin time (*sec*). The total number of calcium peaks above the threshold was added up and normalized by bin time to achieve the event rate. For visualization, smoothing was applied to the event rate map with a 100 mm × 100 mm 2D Gaussian kernel (delta = 20 mm).

2.6.4.   dF/F calculation—When comparing amplitude values, the calcium response of each neuron was normalized to dF/F, which was calculated as $\frac{dF}{F} = \frac{F - F0}{F0}$.

2.6.5.   Information score and place cell—The information score of recorded neurons was calculated as information per second and information per spike introduced by Skaggs et al. (1996). Only the running sessions with speeds larger than 0.5 cm/s were included in the calculation, and the spatial bins with bin time smaller than 0.1 s were excluded to avoid non-existing trespass caused by trajectory smoothing. For a rate map with n bins, the information per event is defined as:

$$Information\ Score(bits/event) = \sum_{i=1}^{n} P_i \frac{\lambda_i}{\lambda} log2 \frac{\lambda_i}{\lambda}$$

P_i is the probability the mouse stays in the i bin, which is represented as the ratio between the bin time and the total time of the trial. λ_i is the event rate of the ith bin, while λ is the average event rate across the trial. A place cell was defined by comparing the information per event of each neuron with its shuffled baseline. The calcium responses were divided into 100 chunks and randomly shuffled 100 times, to disrupt the correspondence with behaviors and generate a distribution of potential score values that the neuron may achieve. A neuron was determined as a place cell if its original score value was higher than the 95th percentile of the shuffled distribution.

2.6.6.   Sparsity—Sparsity is a measure of the fraction of the environment in which the cell is active (Skaggs et al., 1996). The definition is $Sparsity = \frac{\sum (p_i \lambda_i)^2}{\sum p_i \lambda_i^2}$, where p_i is the probability the mouse stays in the ith bin, which is represented as the ratio between the bin time and the total time of the trial, and λ_i is the event rate of the ith bin.

2.6.7.   Spatial coherence—Spatial coherence measures the level of spatially contiguous activity that the neuron exhibits. If the spatial bins with high activity are located close to each other, a high Spatial coherence score would be achieved (Zhang et al., 2014). Spatial coherence was calculated as the Pearson correlation between the activity of every spatial bin and the average activity of its 3 × 3 neighboring bins.

2.6.8.   Statistical analyses—Data are presented as the mean ± s.e.m. unless otherwise specified. Data analysis was conducted using MATLAB and R. Because the data presented in this article were collected using different experimental designs, several appropriate

statistical tests were applied in the data analysis, including the ANOVA, linear mixed-effect model (LME), Kruskal-Wallis and Dunn's post hoc test, Mann-Whitney U test and Kolmogorov-Smirnov test. The LME ("fitlme" in MATLAB) considers correlated data, such as the neurons from the same mouse when conducting statistical modeling and hypothesis testing (Laird and Ware, 1982; Mclean et al., 1991). For example, regarding the comparison between Non-Tg young and AD young mouse cells, measurements of 1180 cells from 5 Non-Tg young mice and 1076 cells from 8 AD young mice are presented in Fig. 3A. We fitted an LME by using a genotype as a fixed effect with mouse id as a random effect. The importance of LME and its more generalized versions has been increasingly recognized in recent studies involving large cell sample data collected from a relatively small number of animals (Indersmitten et al., 2019; Stobart et al., 2018; Yu et al., 2021). For cumulative distributions, the Kolmogorov-Smirnov (KS) test was applied for analysis of the difference. The level of statistical significance was defined as p 0.05.

3. Results

3.1. Age-dependent amyloid-β and tau pathology in 3xTg-AD mice

We used triple-transgenic Alzheimer's disease (3xTg-AD) model mice that overexpress APP_{Swe}, $PS1M_{146V}$ and tau_{P301L} transgenes that contribute to both amyloid-beta (Aβ) plaque and neurofibrillary tangle formation (Belfiore et al., 2019; Oddo et al., 2003). Unlike most other mouse models, 3xTg-AD model mice uniquely develop two AD hallmark pathological features: plaque and tangle formation (Mesulam, 2000; Oddo et al., 2003). To determine age-related and AD progression effects, we compared control and AD-like mice at young and old ages (young age, 3.6–6.5 months old versus old age, 18–21 months old). The age choices are guided by behavioral and neuropathological findings by our and other groups (Baglietto-Vargas et al., 2018; Belfiore et al., 2019; Mesulam, 2000; Oddo et al., 2003; Stimmell et al., 2019).

To measure age-dependent plaque and tau aggregate formation in the AD mouse hippocampus, we immunostained 3xTg-AD and control non-transgenic (Non-Tg) mouse sections with Aβ and Tau antibodies. All hippocampal sample sections were from mice that had undergone imaging and behavioral experiments (see below), thus these results can be correlated with AD neuropathology. Across at least 3 different sets of immunostaining experiments, we confirm that 6.5-month-old 3xTg-AD mice exhibit intracellular Aβ accumulation in hippocampal pyramidal neurons visualized by immunostaining with the 6E10 antibody shown in red, counterstained with DAPI in blue showing cell nuclei (Fig. 1A, bottom left). Extracellular Aβ deposits are distributed throughout the CA1 pyramidal layers and extend to all layers of the hippocampus in 3xTg-AD mice by 18 months (Fig. 1A, bottom right). In contrast, no Aβ deposits are detected in the control Non-Tg mice at either young (Fig. 1A, top left, 6.5 months) or old ages (18 months) (Fig. 1A, top right). The phospho-tau (Ser202, Thr205) monoclonal antibody (AT8) staining, shown in red and counterstained with DAPI shown in blue, was used to identify the presence of human tau pathology in 3 different sets of immunostaining experiments. Anti-AT8 staining shows that tau aggregates in a number of CA1 pyramidal neurons in old 3xTg-AD mice (18-month-old, white arrow, Fig. 1B, bottom right). In comparison, only sparse AT8+ cells are found in

hippocampal CA1 in younger 3xTg-AD mice aged 6.5-months (Fig. 1B, bottom left). Tau pathology is not detected in the young and old control Non-Tg mice (Fig. 1B, top left and right). Consistent with previous work, Aβ accumulation is detectable at an earlier age than tau pathological accumulation in 3xTg-AD mice, and both neuropathological features are absent in age-matched control Non-Tg mice (Belfiore et al., 2019; Oddo et al., 2003). While age-dependent pathological changes correlate with AD-related memory behavioral deficits (Belfiore et al., 2019; Stimmell et al., 2019), spatial coding of in vivo neural circuit activities in the AD mouse model has not been studied during the exploration of environments.

3.2. Miniscope imaging of neural population activities in 3xTg-AD hippocampal CA1

To determine whether hippocampal CA1 ensemble activities during spatial exploration are altered in an age-dependent fashion in 3xTg-AD mice, we used head-mounted miniscopes to image in vivo calcium transient ensemble activities in the 3xTg-AD mouse hippocampal CA1 and compared ensemble activities with age-matched control Non-Tg animals (Fig. 2). To visualize neural calcium activity in the dorsal hippocampal CA1 region, mice were injected with the AAV1-CamKII(0.4)-GCaMP6f virus to restrict expression to CA1 excitatory neurons (Fig. 2A). This 0.4 Kb promoter is derived from murine calcium/ calmodulin-dependent kinase IIα (CaMKIIα) and is reported to show up to 95% specificity to excitatory neurons in the cerebral cortex (Scheyltjens et al., 2015). The hippocampal excitatory neurons are expected to operate as place cells, which is directly relevant to spatial mapping behaviors in AD mouse model (Jun et al., 2020; O'Keefe, 1976; Wilson and McNaughton, 1993). The GCaMP6f expression level in infected neurons did not appear to differ across young or old Non-Tg and 3xTg-AD mice ($N = 6$ mice per genotype, Mann-Whitney U test, $p = 0.6991$) (Fig. S2).

The cortex overlying the hippocampus was removed, then a gradient refractive index (GRIN) lens was implanted above CA1 (Fig. 2B). The implanted GRIN lens allows repeated and longitudinal imaging of the same group of neurons in single cell resolution across prolonged periods up to weeks and months. A small metal baseplate is glued around the lens, and the head-mounted miniscope is magnetically attached to the baseplate. As established in our published studies (Grieco et al., 2021; Grieco et al., 2020; Sun et al., 2019; Wong et al., 2021), GRIN lens implants and the stability of the miniscope attachment permit longitudinal dynamic imaging results to be aligned across sessions and multiple days due to stable registration. Hundreds of neurons can be captured simultaneously in a 700 μm × 450 μm field of view, with a resolution of ~0.9 μm per pixel (Fig. 2C).

Spatial footprints of individual neurons and their corresponding calcium transients were detected and extracted from raw video data using the established CNMF-E method (Zhou et al., 2018a) (Fig. 2C–D). Overall we find that the extracted neuronal numbers in AD mice are less than control mice per the field of view (Fig. 2C), as would be expected due to neurodegenerative impacts. By averaging the numbers of extracted neurons across open field exploration trials, the imaging field in young Non-Tg hippocampal CA1 has more cells in comparison with aged Non-Tg mice (number of neurons: young Non-Tg 653.7 ± 83.7 cells, N = 6 mice; aged Non-Tg, 337.7 ± 44.3 cells, $N = 10$ mice; Kruskal-Wallis test followed by Dunn's post hoc test, $p = 0.0462$). A similar trend is seen in 3xTg AD mice ($p = 0.05$) (Fig.

S1A). The aged group overall has a lower number of extracted neurons than the young group (young group, 520.1 ± 57.3 cells, N = 15 mice; aged group, 312.2 ± 11.2 cells, N = 18 mice, p = 0.0006) (Fig. S1B). This suggests that there are fewer active cells per unit of space in hippocampal CA1 in AD and aging conditions.

To quantitatively characterize hippocampal neuronal ensemble activities during free exploration, we constructed spatial event rate maps for the extracted CA1 neurons during animal exploration in an open circle (diameter, 36 cm) and square (26 cm × 26 cm) arenas. Arenas were divided into 1 cm × 1 cm spatial bins. The binned calcium transient rate is defined by dividing the total number of calcium event peaks by the total exploration times within each bin. Transients as defined by sharp peaks in activity exceeding 10% of the maximum peak amplitude. The spatial event rate maps of example neurons of both ages and genotypes are shown in Fig. 2E–H. For Non-Tg mice at both ages, individual excitatory CA1 neurons are able to display calcium activities restricted to specific locations, which is consistent with the well-described 'place-specific' action potential firing of CA1 excitatory neurons (Fig. 2E, G). For 3xTg-AD mice at both ages, individual excitatory CA1 neurons show less place-specific activities as characterized by more spatially diffuse calcium events (Fig. 2F, H), which suggests decreased signal-to-noise and potential impairment of spatial representation in CA1.

3.3. Age- and AD- dependent neural activity differences in mouse hippocampal CA1 during open field exploration

To further quantitatively investigate the AD- and age-related differences in hippocampal excitatory CA1 neuron activities, we compared the calcium transient rates and calcium event amplitudes of hippocampal CA1 neurons from 3xTg-AD and Non-Tg genotypes at different ages (Fig. 2D, Fig. 3A and B). For the young age group, overall the 3xTg-AD genotype displays a significantly higher calcium event rate compared with the Non-Tg control (Fig. 2E–F, Fig. 3A. Non-Tg young: 0.0752 ± 0.0010 Hz (1180 cells from 5 mice); AD young: 0.0965 ± 0.0013 Hz (1076 cells from 8 mice); linear mixed-effects (LME) model analysis: p = 0.0091). Similarly, for the old age group, on average the old AD mice exhibit a higher event rate than old Non-Tg mice (Fig. 2G–H, Fig. 3A. Non-Tg old: 0.0497 ± 0.0012 Hz (716 cells from 9 mice); 3xTg-AD old: 0.0612 ± 0.0018 Hz (430 cells from 8 mice); LME: p = 0.0094). We also note that for both control and 3xTg-AD mice, age decreases the overall rate of excitatory neural calcium activities in mouse CA1 (Non-Tg young vs. Non-Tg old, LME: p = 3.8744 × 10^{-5}; 3xTg-AD young vs. 3xTg-AD old, LME: p = 1.5095 × 10^{-5}).

In terms of the overall calcium event amplitudes (F/F), we find that 3xTg-AD mice exhibit lower amplitudes than Non-Tg mice at the young age (Fig. 2E–F, Fig. 3B. Non-Tg young: 7.386 ± 0.100 in the unit of dF/F (1180 cells from 5 mice); 3xTg-AD young: 5.725 ± 0.064 dF/F, (1076 cells from 8 mice), LME: p = 0.0066). The calcium amplitudes are generally higher for the old age group, compared with the young age group (Fig. 2G–H, Fig. 3B. Non-Tg old: 11.680 ± 0.322 dF/F (716 cells from 9 mice); 3xTg-AD old: 11.700 ± 0.619 dF/F (430 cells from 8 mice). Non-Tg young vs. Non-Tg old: LME: p = 0.0055, 3xTg-AD young vs. 3xTg-AD old: LME: p = 0.0287). The 3xTg-AD and Non-Tg genotypes did not differ significantly at the old age (LME: p = 0.6388).

These data suggest that 3xTg-AD mouse hippocampal circuits are associated with higher neural ensemble activities relative to Non-Tg controls at either age, which is supported by neural circuit hyperactivity with the accumulation of Aβ as observed in anesthetized AD mouse preparations (Busche et al., 2012; De Strooper and Karran, 2016; Harris et al., 2020).

3.4. Spatial coding impairments of 3xTg-AD CA1 neurons during open field exploration

Given that 3xTg-AD mice show hippocampal spatial memory impairments (Baglietto-Vargas et al., 2018; Oddo et al., 2003; Stimmell et al., 2019), we next investigated the differences of CA1 neuron spatial coding abilities between 3xTg-AD and Non-Tg genotypes at different ages. Using tetrode electrical recordings, a previous study using a different AD mouse model (single APP knock-in, APP-KI) shows that the APP-KI mice exhibit deteriorated spatial tuning represented by lower information score values (Jun et al., 2020). We used a similar approach by calculating the information scores in bits/event from pooled CA1 place cells of each genotype and age group and comparing their cumulative distributions. The bits/event metric is increased when a subset of positional event rates are high against a low mean positional event rate. Because of this, neurons with the place specific activity tend to have high bits/event values.

We find spatial coding impairments of 3xTg-AD hippocampal CA1 neurons in freely moving animals during open-field exploration. The bits/event metric shows that neural calcium events of the 3xTg-AD mice encode less information than Non-Tg mice, at both young and old ages (Fig. 3C; the respective 50%-cumulative values for Non-Tg young (233 place cells from 5 mice), AD young (214 place cells from 8 mice), Non-Tg old (104 place cells from 9 mice) and 3xTg-AD old (131 place cells from 8 mice) are 3.4681, 3.0372, 4.2743 and 3.4172. Non-Tg young vs. 3xTg-AD young distributions: $p = 4.1683 \times 10^{-12}$. Non-Tg old vs. 3xTg-AD old: $p = 5.2701 \times 10^{-7}$, Non-Tg young vs. Non-Tg old: $p = 6.3021 \times 10^{-12}$, 3xTg-AD young vs. 3xTg-AD old: $p = 1.1370 \times 10^{-6}$, two-sample Kolmogorov-Smirnov test).

To further compare the spatial coding abilities of hippocampal CA1 excitatory neurons across the genotype and age groups, we measured the sparsity and spatial coherence (Jung et al., 1994; Zhang et al., 2014) of calcium event rate maps for all CA1 neurons pooled from each mouse group. The sparsity index measures the fraction of the exploration area where a neuron fires spikes, and lower sparsity indicates more constrained firing activities at specific locations (Jung et al., 1994). Coherence measures the extent to which adjacent positional bins share similar event rates. For place-specific activity, coherence is high because spatial bins with high rates are concentrated in one location. We find that at either age, 3xTg-AD CA1 cells exhibit higher sparsity values than Non-Tg, which complements the bits/event measures and indicates the lower spatial selectivity of cell firing in 3xTg-AD mice (Fig. 3D; the respective 50%-cumulative values for Non-Tg young (1180 cells from 5 mice), 3xTg-AD young (1076 cells from 8 mice), Non-Tg old (716 cells from 9 mice), and 3xTg-AD old (430 cells from 8 mice) are 0.0746, 0.0957, 0.0492 and 0.0657. Non-Tg young vs. 3xTg-AD young: $p = 1.2703 \times 10^{-31}$, Non-Tg old vs. 3xTg-AD old: $p = 2.0458 \times 10^{-7}$, two-sample Kolmogorov-Smirnov test). Further, for both 3xTg-AD and Non-Tg, mice in the young age group have a higher sparsity than the old age group (Fig. 3D; Non-Tg young vs. Non-Tg

old: $p = 9.0277 \times 10^{-42}$; 3xTg-AD young vs. 3xTg-AD old: $p = 1.0343 \times 10^{-25}$, two-sample Kolmogorov-Smirnov test). In addition, the 3xTg-AD mice show overall higher coherence values of activity rate maps than Non-Tg mice at the old age (Fig. 3E; the respective 50%-cumulative- values for Non-Tg young (1180 cells from 5 mice), 3xTg-AD young (1076 cells from 8 mice), Non-Tg old (716 cells from 9 mice), and 3xTg-AD old (430 cells from 8 mice): 0.4369, 0.4437, 0.4123 and 0.4286. Non-Tg young vs. 3xTg-AD young: $p = 0.0728$, Non-Tg old vs. 3xTg-AD old: $p = 5.4990 \times 10^{-4}$, two-sample Kolmogorov-Smirnov test). Younger mice show higher coherence than older mice for both genotypes (Fig. 3E; Non-Tg young vs. Non-Tg old: $p = 2.3031 \times 10^{-6}$, 3xTg-AD young vs. 3xTg-AD old: $p = 0.0177$, two-sample Kolmogorov-Smirnov test). As spatial coherence measures the correlation between the activity of each bin and the averaged activities of its neighborhood bins in a rate map (Jung et al., 1994), we reason that the more diffuse firing fields of old 3xTg-AD mice may result in higher spatial coherence.

3.5. Spatial coding deficits of 3xTg-AD CA1 neurons in linear track trials

We extended our investigation to a linear track environment. Population calcium transient activities in hippocampal CA1 were imaged with miniscopes while mice ran along a 1-m linear track (width, 3 cm) for a water reward at each end. To consider the direction-dependent neural activities, we analyzed calcium transient data in two running directions. CA1 excitatory neurons that exhibit place selective activities can be identified from the populations across the genotypes and ages (Fig. 4A–D). We quantitatively analyzed the place-specific activities in linear track trials, as we did for open-field exploration. We find that the calcium event rates across mouse groups do not exhibit significant differences (Fig. 4E), but AD mice show a significant difference from Non-Tg mice in terms of calcium event amplitudes (Fig. 4F; Non-Tg young (1742 cells from 6 mice): 5.745 ± 0.112 dF/F; 3xTg-AD young (1988 cells from 8 mice): 4.534 ± 0.076 dF/F; Non-Tg old (1136 cells from 5 mice): 4.573 ± 0.107 dF/F; 3xTg-AD old (1560 cells from 5 mice): 5.064 ± 0.079 dF/F. Non-Tg young vs. 3xTg-AD young, LME: $p = 0.0167$; Non-Tg old vs. 3xTg-AD old, LME: $p = 0.0495$; Non-Tg young vs. Non-Tg old, LME: $p = 0.0132$; 3xTg-AD young vs. 3xTg-AD old, LME: $p = 0.0354$).

Consistent with our finding in mouse exploration of open fields, we find that for both ages, 3xTg-AD mice exhibit lower spatial information score in bits/event than Non-Tg mice (Fig. 4G; the respective 50%-cumulative values for Non-Tg young (238 place cells in direction 1 + 246 place cells in direction 2, from 6 mice), 3xTg-AD young (213 place cells in direction 1 + 237 place cells in direction 2, from 8 mice), Non-Tg old (163 place cells in direction 1 + 159 place cells in direction 2, from 5 mice) and 3xTg-AD old are (259 place cells in direction 1 + 272 place cells in direction 2, from 5 mice) are 2.8194, 2.6591, 2.2647 and 1.9509. Non-Tg young vs. 3xTg-AD young: $p = 0.0432$, Non-Tg old vs. 3xTg-AD old: $p = 0.0010$, Non-Tg young vs. Non-Tg old: $p = 8.7241 \times 10^{-7}$, 3xTg-AD young vs. 3xTg-AD old: $p = 3.4423 \times 10^{-5}$, two-sample Kolmogorov-Smirnov test).

During linear track trials, hippocampal CA1 excitatory neurons in old 3xTg-AD mice have higher sparsity values than young 3xTg-AD mice, while for control mice, there are no significant differences between ages (Fig. 4H; the respective 50%-cumulative values for

Non-Tg young (1742 cells (each direction) from 6 mice), 3xTg-AD young (1988 cells (each direction) from 8 mice), Non-Tg old (1136 cells (each direction) from 5 mice) and 3xTg-AD old (1560 cells (each direction) from 6 mice) are 0.0490, 0.0429, 0.0499, and 0.0559. Non-Tg young vs. 3xTg-AD young: $p = 1.2231 \times 10^{-9}$, Non-Tg old vs. 3xTg-AD old: $p = 1.7939 \times 10^{-5}$, Non-Tg young vs. Non-Tg old: $p = 0.0818$; 3xTg-AD young vs. 3xTg-AD old: $p = 3.4707 \times 10^{-31}$, two-sample Kolmogorov-Smirnov test). 3xTg-AD mouse cells exhibit higher spatial coherence values than Non-Tg mice (Fig. 4I; the respective 50%-cumulative values for Non-Tg young (1742 cells (each direction) from 6 mice), 3xTg-AD young (1988 cells (each direction) from 8 mice), Non-Tg old (1136 cells (each direction) from 5 mice) and, 3xTg-AD old (1560 cells (each direction) from 6 mice) are 0.3573, 0.3658, 0.3632 and 0.3778. Non-Tg young vs. 3xTg-AD young: $p = 8.8051 \times 10^{-10}$, Non-Tg old vs. 3xTg-AD old: $p = 2.7640 \times 10^{-11}$, Non-Tg young vs. Non-Tg old: $p = 7.9276 \times 10^{-12}$, 3xTg-AD young vs. 3xTg-AD old: $p = 2.7437*10^{-17}$, two-sample Kolmogorov-Smirnov test).

3.6. Locomotion modulation of 3xTg-AD mouse CA1 neural population activities

It is known that locomotion states have significant effects across rodent sensory systems including visual and auditory circuits (Arriaga and Han, 2017a). While both the calcium activities of CA1 excitatory neurons and inhibitory neurons can be modulated by locomotion (Fuhrmann et al., 2015; Góis and Tort, 2018), locomotion effects on hippocampal neural calcium population activities have not yet been studied in freely moving animals. Miniscope imaging has the advantage of monitoring neural ensemble activities in hippocampal CA1 of animals during free moving conditions, thus providing the opportunity to examine the modulatory effects of free locomotion on CA1 neural calcium activity ensembles across different groups.

As shown in Fig. 5A, the calcium activities of hundreds of excitatory neurons recorded during one session from each example mouse are displayed in raster plots over the exploration time. We delineate the high-velocity epochs (black vertical bars) below the raster plots to enable visual comparisons between the neural activity level and locomotion velocity. The high-velocity epoch is defined as the duration when the velocity goes above the averaged trial velocities of each group (Fig. 5B). To further illustrate the relationship between population calcium responses and velocity over time, we align the z-scored ensemble calcium response trace with the z-scored velocity trace. Interestingly, compared with control mice at young or old age, overall neural population calcium activities in hippocampal CA1 of AD mice appear to be more closely modulated by locomotion velocities and CA1 ensemble amplitudes are positively correlated with locomotion velocity changes (Fig. 5A).

We quantitatively examined the relationship between calcium activity amplitude and velocity by calculating the correlation between individual neurons' calcium responses and velocities. We apply a 15 s Gaussian window (2.5 s standard deviation) to smooth both calcium response and movement velocity traces in the time-series, then compare the cumulative distributions of correlations across different genotypes and ages. Our quantification confirms our qualitative observations in Fig. 5A. Compared with age-matched controls, young and old 3xTg-AD CA1 neurons show stronger correlations between calcium

response amplitudes and locomotion velocities (Fig. 5C; the respective 50%-cumulative values for Non-Tg young (1180 cells from 5 mice), 3xTg-AD young (1076 cells from 8 mice), Non-Tg old (716 cells from 9 mice), and 3xTg-AD old (430 cells from 8 mice) are 0.0435, 0.0561, 0.0341 and 0.093. Non-Tg young vs. 3xTg-AD young: $p = 9.2871 \times 10^{-6}$, Non-Tg old vs. 3xTg-AD old: $p = 1.6663 \times 10^{-10}$, two-sample Kolmogorov-Smirnov test). This holds true when we only include place cells for analysis. Place cells were defined as cells with spatial information scores above the chance level (see details in the Methods). The locomotion effects appear to be more robust for the place cells (Fig. 5D; the respective 50%-cumulative values for Non-Tg young (233 place cells from 5 mice), 3xTg-AD young (214 place cells from 5 mice), Non-Tg old (104 place cells from 9 mice), and 3xTg-AD old (131 place cells from 5 mice) are 0.1228, 0.1560, 0.0901 and 0.1556. Non-Tg young vs. 3xTg-AD young: $p = 0.0093$, Non-Tg old vs. 3xTg-AD old: $p = 0.0016$, two-sample Kolmogorov-Smirnov test).

4. Discussion

Previous work on AD has focused on molecular and neuropathological features as they correlate with cognitive defects. AD research is now increasingly focused on mechanistic changes at the level of neuronal circuits (Harris et al., 2020). In the present study, we have examined neural calcium activities of hippocampal CA1 neuronal populations in freely behaving 3xTg-AD mice and controls at young and old ages. We leveraged the advantages of miniscope-based GCaMP calcium imaging to examine the impairments of spatial representation and spatial coding by comparing hippocampal CA1 excitatory neural ensemble activities during open-field exploration, and track-based route-running behaviors in age-matched AD and control mice. We have identified AD- and age-related differences in neural calcium activities, and have determined deficits in spatial information coding in hippocampal neural ensembles in the 3xTg-AD mouse model. We also find locomotion significantly modulates the amplitude of hippocampal neural ensemble activities in 3xTg-AD mice, but not in non-transgenic controls during open-field exploration.

Many transgenic AD models have been used in the research studies to date, but most models only contain mutation genes for the progression of Aβ plaques, such as APP Tg2576, APP/PS1 and 5xFAD. These models are convenient for the detection of Aβ accumulation at an early age but do not take into account the tau pathology in the late AD stage. In our study, we used the 3xTg-AD mouse model that contains the genetic mutations contributing to both pathological markers (Mesulam, 2000; Oddo et al., 2003). AD-related neurodegeneration may affect hippocampal CA1 neural activation as 3xTg-AD hippocampal CA1 imaging fields have a smaller number of extracted neurons compared to control mouse hippocampal CA1 fields. Aging might also have effects, as the aged group also has a lower number of extracted neurons relative to the young group. The age-dependent plaque and tau aggregate formation in the 3xTg-AD mouse hippocampus is correlated well with CA1 neural activity alterations identified in our imaging experiments across the ages and genotypes. Our imaging results are also supported by the deficiency in spatial memory behaviors observed in 3xTg-AD mice (Baglietto-Vargas et al., 2018; Oddo et al., 2003; Stimmell et al., 2019).

We identify AD- and age- dependent neural activity differences in mouse hippocampal CA1 during open-field exploration. We find that 3xTg-AD CA1 excitatory cells have significantly higher calcium event rates compared with controls at both young or old ages, indicating that in vivo enhanced neuronal ensemble activity is a disease feature. The absence of this effect during linear track running suggests that rate changes may be muted under conditions wherein the direction of travel through environmental locations is much more regular and for which proximal cues to define environmental locations are continuously present. Our data show the consistent differences of calcium event rates in open field and linear track environments across age and genotype (Fig. S3), supporting this idea. Further work will be needed to disentangle how the structure and richness of environmental cues impacts specific features of network activity in aged and AD model animals.

We also examined whether calcium event amplitudes vary between control and 3xTg-AD in an age-dependent fashion. Old 3xTg-AD mice exhibit significantly higher calcium event amplitudes relative to young 3xTg-AD. The higher neural ensemble calcium activities (event rates and amplitudes) found in aged 3xtg AD mouse hippocampal CA1 is supported by the finding of neural circuit hyperactivity observed in anesthetized AD mouse preparations (Busche et al., 2012; De Strooper and Karran, 2016; Harris et al., 2020).

Our data demonstrate spatial coding defects of hippocampal CA1 ensemble activities in 3xTg-AD mice, as our overall imaging results in both open field and linear track environments indicate that neuronal populations of 3xTg-AD mice show lower spatial information scores compared with control mice at both young and old ages. The spatial firing of CA1 neurons of old 3xTg-AD mice also displays higher sparsity and increased coherence, effects consistent with an overall decrease in the tuning of activity to single locations. This supports the notion that place-specific firing fields of CA1 neurons in the AD condition tend to be larger in size, which indicates less place specificity for spatial representation. Additionally, it would also be important to examine ensemble coding stability as well as calcium activity-based decoding accuracy using computational models. We plan to address this as a future direction.

Our finding that locomotion significantly modulates the amplitude of hippocampal neural ensemble activities in 3xTg-AD mice, but not in non-transgenic controls is another important new finding. During movement, hippocampal local field potential (LFP) activity is characterized by θ-frequency oscillations; in contrast, during awake immobility, LFP activity is interspersed by large, irregular activity containing periods of sharp-wave/ripple (SWR) events. Much current research related to this is focused on hippocampal interneurons as their activity is highly modulated with locomotion speed (Arriaga and Han, 2017b; Góis and Tort, 2018), while locomotion modulates excitatory neurons to a lesser degree (Góis and Tort, 2018). Given that AD neurodegeneration can alter circuit excitation/inhibition balance, it can be inferred that the speed-correlated inhibition of pyramidal neurons will be weakened in the AD condition. Indeed, our results indicate that CA1 place cells from 3xTg-AD mice exhibit obviously stronger speed modulation on their neural calcium activity amplitudes. Whether a decrease in inhibition will lead to higher activity modulation of excitatory neurons in AD-related neural circuits requires further investigation.

5. Conclusions

In conclusion, we applied miniscope calcium imaging in the 3xTg-AD model and control mice to determine the AD- and aging-related impacts on hippocampal neural population activities. Our data show neural activity alterations and spatial coding defects in CA1 neuronal ensembles that correlate with the development of AD pathology and AD-related spatial memory behavioral deficits.

Supplementary Material

Refer to Web version on PubMed Central for supplementary material.

Acknowledgments

Availability of data and materials

The datasets used for the present study are available from the corresponding author upon reasonable request.

Abbreviations:

3xTg-AD	Triple-transgenic Alzheimer's disease mouse model
5xFAD	Five familial Alzheimer's disease (FAD) mutations
AAV	Adeno-associated virus
AD	Alzheimer's disease
AP	Anteroposterior
APP-KI	Amyloid precursor protein-knock in mouse model
Aβ	amyloid-beta
CaMKII	Calcium/calmodulin-dependent kinase II
CNMF-E	Extended Constrained Nonnegative Matrix Factorization
DV	Dorsoventral
GRIN	Gradient refractive index
KS	Kolmogorov-Smirnov
LME	linear mixed-effect model

Miniscopes	Miniature fluorescent microscopes
ML	Mediolateral
Non-Tg	Non-transgenic
OASIS	Online Active Set method to Infer Spikes
PBS	Phosphate buffered saline
ROI	Region of interest
SUB	Subiculum

References

Alzheimer's Association, 2020. Alzheimer's disease facts and figures. Alzheimer's Association. https://www.alz.org/alzheimers-dementia/facts-figures.

Arriaga M, Han EB, 2017a. Dedicated hippocampal inhibitory networks for locomotion and immobility. J. Neurosci. 37, 9222–9238. [PubMed: 28842418]

Arriaga M, Han EB, 2017b. Dedicated hippocampal inhibitory networks for locomotion and immobility. J. Neurosci. 37, 9222. [PubMed: 28842418]

Baglietto-Vargas D, Prieto GA, Limon A, Forner S, Rodriguez-Ortiz CJ, Ikemura K, Ager RR, Medeiros R, Trujillo-Estrada L, Martini AC, et al. , 2018. Impaired AMPA signaling and cytoskeletal alterations induce early synaptic dysfunction in a mouse model of Alzheimer's disease. Aging Cell 17, e12791. [PubMed: 29877034]

Bast T, Pezze M, McGarrity S, 2017. Cognitive deficits caused by prefrontal cortical and hippocampal neural disinhibition. Br. J. Pharmacol. 174, 3211–3225. [PubMed: 28477384]

Belfiore R, Rodin A, Ferreira E, Velazquez R, Branca C, Caccamo A, Oddo S, 2019. Temporal and regional progression of Alzheimer's disease-like pathology in 3xTg-AD mice. Aging Cell 18, e12873. [PubMed: 30488653]

Billings LM, Oddo S, Green KN, McGaugh JL, LaFerla FM, 2005. Intraneuronal Abeta causes the onset of early Alzheimer's disease-related cognitive deficits in transgenic mice. Neuron 45, 675–688. [PubMed: 15748844]

Busche MA, Konnerth A, 2016. Impairments of neural circuit function in Alzheimer's disease. Philos. Trans. R. Soc. Lond. B 371.

Busche MA, Chen X, Henning HA, Reichwald J, Staufenbiel M, Sakmann B, Konnerth A, 2012. Critical role of soluble amyloid-beta for early hippocampal hyperactivity in a mouse model of Alzheimer's disease. Proc. Natl. Acad. Sci. U. S. A. 109, 8740–8745. [PubMed: 22592800]

Cai DJ, Aharoni D, Shuman T, Shobe J, Biane J, Song W, Wei B, Veshkini M, La-Vu M, Lou J, et al. , 2016. A shared neural ensemble links distinct contextual memories encoded close in time. Nature 534, 115–118. [PubMed: 27251287]

Carroll JC, Rosario ER, Kreimer S, Villamagna A, Gentzschein E, Stanczyk FZ, Pike CJ, 2010. Sex differences in beta-amyloid accumulation in 3xTg-AD mice: role of neonatal sex steroid hormone exposure. Brain Res. 1366, 233–245. [PubMed: 20934413]

Cembrowski MS, Phillips MG, DiLisio SF, Shields BC, Winnubst J, Chandrashekar J, Bas E, Spruston N, 2018. Dissociable structural and functional hippocampal outputs via distinct subiculum cell classes. Cell 174, 1036. [PubMed: 30096303]

Chen TW, Wardill TJ, Sun Y, Pulver SR, Renninger SL, Baohan A, Schreiter ER, Kerr RA, Orger MB, Jayaraman V, et al. , 2013. Ultrasensitive fluorescent proteins for imaging neuronal activity. Nature 499, 295–300. [PubMed: 23868258]

De Strooper B, Karran E, 2016. The cellular phase of Alzheimer's disease. Cell 164, 603–615. [PubMed: 26871627]

Frere S, Slutsky I, 2018. Alzheimer's disease: from firing instability to homeostasis network collapse. Neuron 97, 32–58. [PubMed: 29301104]

Friedrich J, Zhou P, Paninski L, 2017. Fast online deconvolution of calcium imaging data. PLoS Comput. Biol. 13, e1005423. [PubMed: 28291787]

Fuhrmann F, Justus D, Sosulina L, Kaneko H, Beutel T, Friedrichs D, Schoch S, Schwarz MK, Fuhrmann M, Remy S, 2015. Locomotion, theta oscillations, and the speed-correlated firing of hippocampal neurons are controlled by a medial septal glutamatergic circuit. Neuron 86, 1253–1264. [PubMed: 25982367]

Góis ZHTD, Tort ABL, 2018. Characterizing speed cells in the rat hippocampus. Cell Rep. 25, 1872–1884.e1874. [PubMed: 30428354]

Grieco SF, Qiao X, Zheng X, Liu Y, Chen L, Zhang H, Yu Z, Gavornik JP, Lai C, Gandhi SP, et al. , 2020. Subanesthetic ketamine reactivates adult cortical plasticity to restore vision from amblyopia. Curr. Biol. 30 (3591–3603), e3598.

Grieco SF, Qiao X, Johnston KG, Chen L, Nelson RR, Lai C, Holmes TC, Xu X, 2021. Neuregulin signaling mediates the acute and sustained antidepressant effects of subanesthetic ketamine. Transl. Psychiatry 11, 144. [PubMed: 33627623]

Grienberger C, Rochefort NL, Adelsberger H, Henning HA, Hill DN, Reichwald J, Staufenbiel M, Konnerth A, 2012. Staged decline of neuronal function in vivo in an animal model of Alzheimer's disease. Nat. Commun. 3, 774. [PubMed: 22491322]

Harris SS, Wolf F, De Strooper B, Busche MA, 2020. Tipping the scales: peptide-dependent dysregulation of neural circuit dynamics in Alzheimer's disease. Neuron 107, 417–435. [PubMed: 32579881]

Indersmitten T, Schachter MJ, Young S, Welty N, Otte S, Nassi JJ, Lovenberg T, Bonaventure P, Wyatt RM, 2019. In vivo calcium imaging reveals that cortisol treatment reduces the number of place cells in Thy1-GCaMP6f transgenic mice. Front. Neurosci. Switz. 13.

Jun H, Bramian A, Soma S, Saito T, Saido TC, Igarashi KM, 2020. Disrupted place cell remapping and impaired grid cells in a Knockin model of Alzheimer's disease. Neuron 107 (1095–1112), e1096.

Jung MW, Wiener SI, McNaughton BL, 1994. Comparison of spatial firing characteristics of units in dorsal and ventral hippocampus of the rat. J. Neurosci. 14, 7347–7356. [PubMed: 7996180]

Laird NM, Ware JH, 1982. Random-effects models for longitudinal data. Biometrics 38, 963–974. [PubMed: 7168798]

Lerdkrai C, Asavapanumas N, Brawek B, Kovalchuk Y, Mojtahedi N, Olmedillas Del Moral M, Garaschuk O, 2018. Intracellular Ca(2+) stores control in vivo neuronal hyperactivity in a mouse model of Alzheimer's disease. Proc. Natl. Acad. Sci. U. S. A. 115, E1279–E1288. [PubMed: 29358403]

Mclean RA, Sanders WL, Stroup WW, 1991. A unified approach to mixed linear-models. Am. Stat. 45, 54–64.

Mesulam MM, 2000. A plasticity-based theory of the pathogenesis of Alzheimer's disease. Ann. N. Y. Acad. Sci. 924, 42–52. [PubMed: 11193801]

Naber PA, Witter MP, Lopes Silva FH, 2000. Networks of the hippocampal memory system of the rat. The pivotal role of the subiculum. Ann. N. Y. Acad. Sci. 911, 392–403. [PubMed: 10911887]

Oddo S, Caccamo A, Shepherd JD, Murphy MP, Golde TE, Kayed R, Metherate R, Mattson MP, Akbari Y, LaFerla FM, 2003. Triple-transgenic model of Alzheimer's disease with plaques and tangles: intracellular Abeta and synaptic dysfunction. Neuron 39, 409–421. [PubMed: 12895417]

O'Keefe J, 1976. Place units in the hippocampus of the freely moving rat. Exp. Neurol. 51, 78–109. [PubMed: 1261644]

Palop JJ, Mucke L, 2016. Network abnormalities and interneuron dysfunction in Alzheimer disease. Nat. Rev. Neurosci. 17, 777–792. [PubMed: 27829687]

Pnevmatikakis EA, Giovannucci A, 2017. NoRMCorre: an online algorithm for piecewise rigid motion correction of calcium imaging data. J. Neurosci. Methods 291, 83–94. [PubMed: 28782629]

Scheyltjens I, Laramee ME, Van den Haute C, Gijsbers R, Debyser Z, Baekelandt V, Vreysen S, Arckens L, 2015. Evaluation of the expression pattern of rAAV2/1, 2/5, 2/7, 2/8, and 2/9 serotypes with different promoters in the mouse visual cortex. J. Comp. Neurol. 523, 2019–2042. [PubMed: 26012540]

Selkoe DJ, 2002. Alzheimer's disease is a synaptic failure. Science 298, 789–791. [PubMed: 12399581]

Shinohara Y, Hosoya A, Yamasaki N, Ahmed H, Hattori S, Eguchi M, Yamaguchi S, Miyakawa T, Hirase H, Shigemoto R, 2012. Right-hemispheric dominance of spatial memory in split-brain mice. Hippocampus 22, 117–121. [PubMed: 21069782]

Skaggs WE, McNaughton BL, Wilson MA, Barnes CA, 1996. Theta phase precession in hippocampal neuronal populations and the compression of temporal sequences. Hippocampus 6, 149–172. [PubMed: 8797016]

Stimmell AC, Baglietto-Vargas D, Moseley SC, Lapointe V, Thompson LM, LaFerla FM, McNaughton BL, Wilber AA, 2019. Impaired spatial reorientation in the 3xTg-AD mouse model of Alzheimer's disease. Sci. Rep. 9, 1311. [PubMed: 30718609]

Stobart JL, Ferrari KD, Barrett MJP, Stobart MJ, Looser ZJ, Saab AS, Weber B, 2018. Long-term in vivo calcium imaging of astrocytes reveals distinct cellular compartment responses to sensory stimulation. Cereb. Cortex 28, 184–198. [PubMed: 28968832]

Sun Y, Jin S, Lin X, Chen L, Qiao X, Jiang L, Zhou P, Johnston KG, Golshani P, Nie Q, et al. , 2019. CA1-projecting subiculum neurons facilitate object-place learning. Nat. Neurosci. 22, 1857–1870. [PubMed: 31548723]

Weller J, Budson A, 2018. Current understanding of Alzheimer's disease diagnosis and treatment. F1000Research 7.

Wilson MA, McNaughton BL, 1993. Dynamics of the hippocampal ensemble code for space. Science 261, 1055–1058. [PubMed: 8351520]

Wong JC, Grieco SF, Dutt K, Chen L, Thelin JT, Inglis GAS, Parvin S, Garraway SM, Xu X, Goldin AL, et al. , 2021. Autistic-like behavior, spontaneous seizures, and increased neuronal excitability in a Scn8a mouse model. Neuropsychopharmacology 46, 2011–2020. 10.1038/s41386-021-00985-9. [PubMed: 33658654]

Xu X, Sun Y, Holmes TC, Lopez AJ, 2016. Noncanonical connections between the subiculum and hippocampal CA1. J. Comp. Neurol. 524, 3666–3673. [PubMed: 27150503]

Yang X, Yao C, Tian T, Li X, Yan H, Wu J, Li H, Pei L, Liu D, Tian Q, et al. , 2018. A novel mechanism of memory loss in Alzheimer's disease mice via the degeneration of entorhinal-CA1 synapses. Mol. Psychiatry 23, 199–210. [PubMed: 27671476]

Yu Z, Guindani M, Grieco S, Chen L, Holmes T, Xu X, 2021. Beyond t test and ANOVA: applications of mixed-effects models for more rigorous statistical analysis in neuroscience research. Neuron. 10.1016/j.neuron.2021.10.030.

Zhang S, Schonfeld F, Wiskott L, Manahan-Vaughan D, 2014. Spatial representations of place cells in darkness are supported by path integration and border information. Front. Behav. Neurosci. 8, 222. [PubMed: 25009477]

Zhou P, Resendez SL, Rodriguez-Romaguera J, Jimenez JC, Neufeld SQ, Giovannucci A, Friedrich J, Pnevmatikakis EA, Stuber GD, Hen R, et al. , 2018a. Efficient and accurate extraction of in vivo calcium signals from microendoscopic video data. eLife 7, e28728. [PubMed: 29469809]

Zhou P, Resendez SL, Rodriguez-Romaguera J, Jimenez JC, Neufeld SQ, Giovannucci A, Friedrich J, Pnevmatikakis EA, Stuber GD, Hen R, et al. , 2018b. Efficient and accurate extraction of in vivo calcium signals from microendoscopic video data. eLife 7.

Ziv Y, Burns LD, Cocker ED, Hamel EO, Ghosh KK, Kitch LJ, El Gamal A, Schnitzer MJ, 2013. Long-term dynamics of CA1 hippocampal place codes. Nat. Neurosci. 16, 264–266. [PubMed: 23396101]
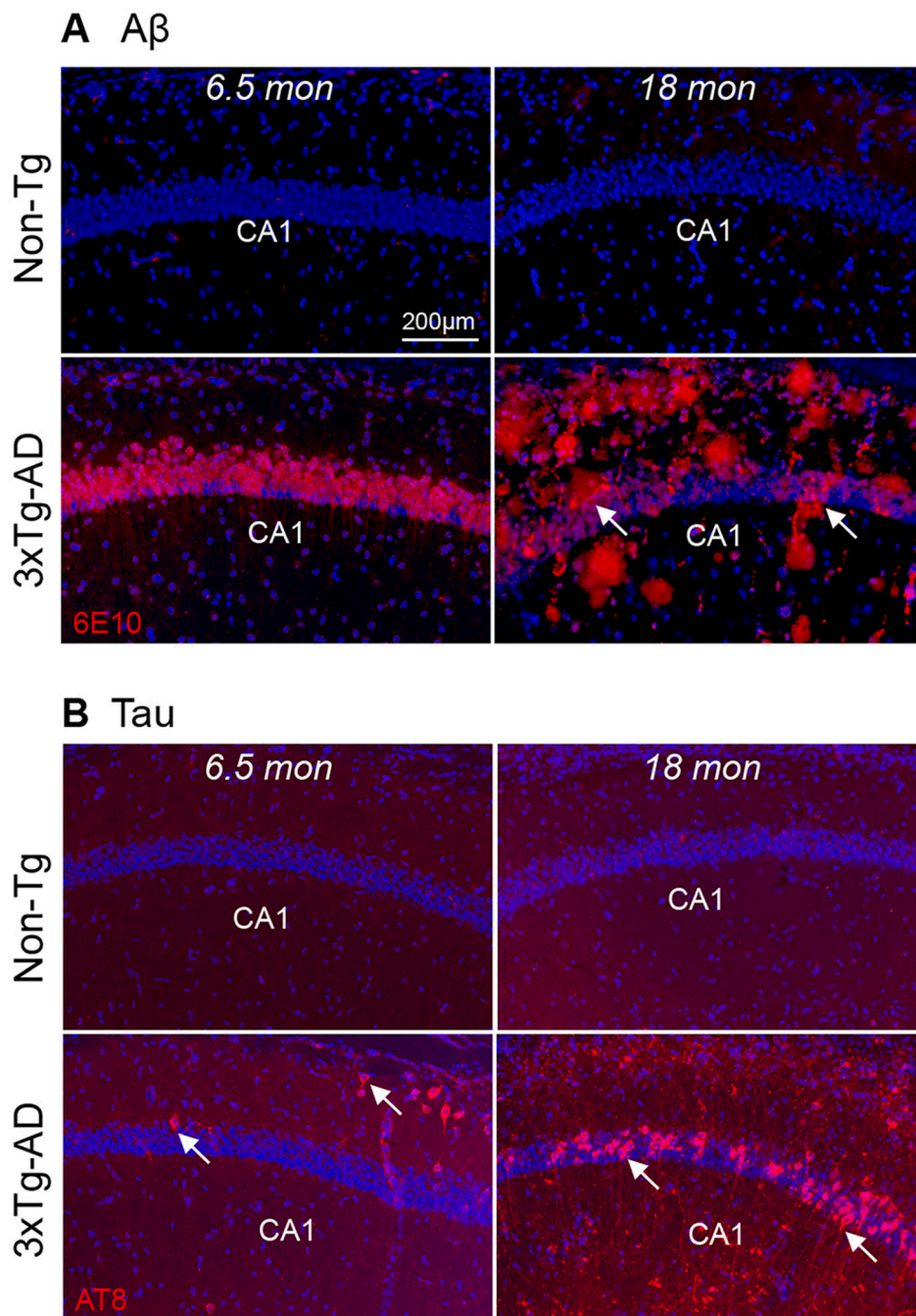
Fig. 1.
Age-dependent change in amyloid beta (Aβ) and phospho-tau accumulation in 3xTg-AD mouse hippocampus. A. Comparison of Aβ pathology in the 6.5-month-old and 18-month-old 3xTg-AD and control, Non-Tg mice. 6.5-month-old 3xTg-AD mice show intraneuronal Aβ staining in the pyramidal layer of hippocampal CA1 (left bottom panels). Aβ staining is red and DAPI staining is blue. The accumulation of Aβ (plaques, arrows) is distributed across all the layers of hippocampal CA1 in an 18-month-old 3xTg-AD mouse (bottom right panel) as compared to a non-transgenic control mouse (Non-Tg) (top right panel). B.

Phospho-tau builds up in the 3xTg-AD mouse hippocampus. Tau staining is red. 6.5 months old 3xTg-AD (bottom left) mice show sparsely tau labeling in distal CA1. The 18-month-old group exhibits elevated tau pathology in hippocampal CA1 pyramidal cells (arrows) (bottom right). The Non-Tg (top two panels) mouse hippocampus does not develop tau pathology. Scale bar = 200 μm.
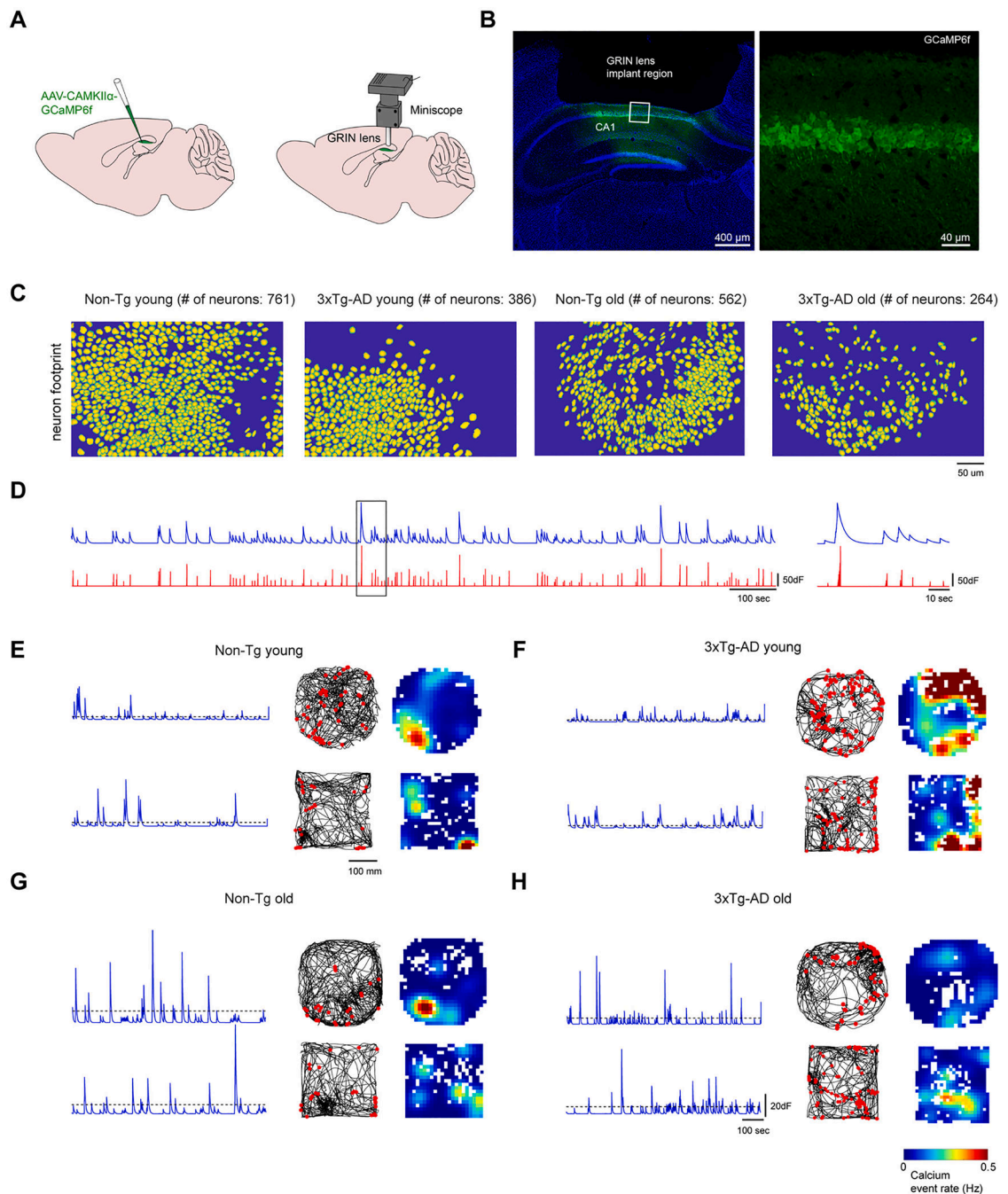
Fig. 2.
In vivo neural calcium imaging of hippocampal CA1 excitatory neurons in 3xTg-AD and Non-Tg mice. A. The scheme for viral injection and miniaturized fluorescent microscope (miniscope) recording in the hippocampal CA1 region. A 1.8-mm diameter GRIN lens (shown in grey) was implanted at the same location as the AAV1 injection site for in vivo calcium signal recording in the behaving animal. B. A coronal section image shows the location for GRIN lens implantation in hippocampal CA1. DAPI staining is blue. GCaMP6f signal is green. Scale bar = 400 μm. Right panel: the higher magnification image of the

left panel. The GCaMP6f infected cells are restricted to the pyramidal layers of the CA1 region. Scale bar = 40 μm. C. Examples of neuron footprints from CNMF-E extraction for data processing. Left to right, examples are from young Non-Tg, young 3xTg-, old Non-Tg and old 3xTg-AD, respectively. D. Extracted calcium signal traces. The blue trace represents the calcium signal and the corresponding deconvoluted trace is plotted below (red). The magnified calcium signal trace from the black box (left) is shown on the right. *E*-H. 3xTg-AD CA1 cells exhibit less place-specific firing properties compared to Non-Tg CA1 cells during open field exploration. E. Example neural calcium signals and spatial rate maps of calcium events from a young Non-Tg mouse. Left: Denoised calcium signal of one neuron. Middle: travel trajectory in the circular arena is plotted by the black line. Red dots represent the locations in which the calcium events are higher than the threshold. Right: Rate maps of calcium events. The arena is divided into 10×10 mm bins and each bin's event rate is calculated as the total number of events divided by the total time that the mouse spends inside the bin. The rate map is smoothed with 100×100 mm Gaussian kernel (standard deviation = 20 mm). F, G, H are arranged in the same format for old-age Non-Tg, young-age 3xTg-AD and old-age 3xTg-AD mice.
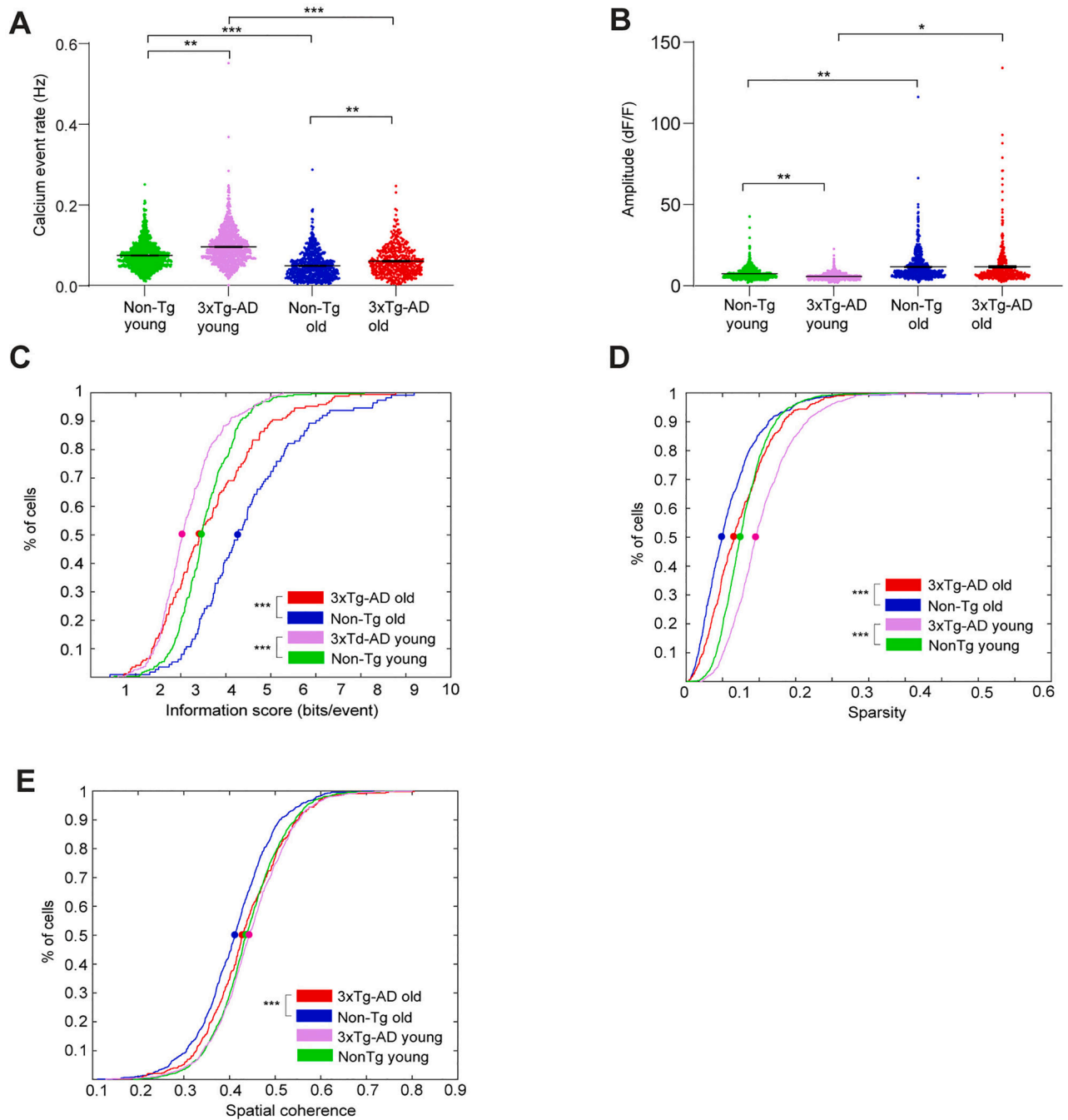
Fig. 3.
3xTg-AD CA1 cells exhibit altered calcium activities and impaired spatial coding during open field exploration. A. Violin plots of calcium event rates of all neurons from different groups of mice. Only the periods with movement speeds higher than 5 mm/s were used for event rate calculation, and event rates from trials within arenas of the same geometry were averaged. B. Violin plots of calcium event amplitudes of all neurons from different groups of mice. C. Cumulative distribution plots of spatial information scores (in bits/event) for all place cells from Non-Tg old, 3xTg-AD old, Non-Tg young and 3xTg-AD young

mice exploring in both square and circle arenas. D. Cumulative distribution plots of sparsity values of all neurons for all Non-Tg old, 3xTg-AD old, Non-Tg young and 3xTg-AD young mice in both square and circular arenas. E. Cumulative distribution plots of spatial coherence values of all neurons for all Non-Tg old, 3xTg-AD old, Non-Tg young and 3xTg-AD young mice, in both square and circular arenas. LME analyses were used for A-B; two-sample Kolmogorov-Smirnov tests were used for C-E. *, ** and *** indicate the significance levels with the respective p values of <0.05, <0.005, and < 0.0005.
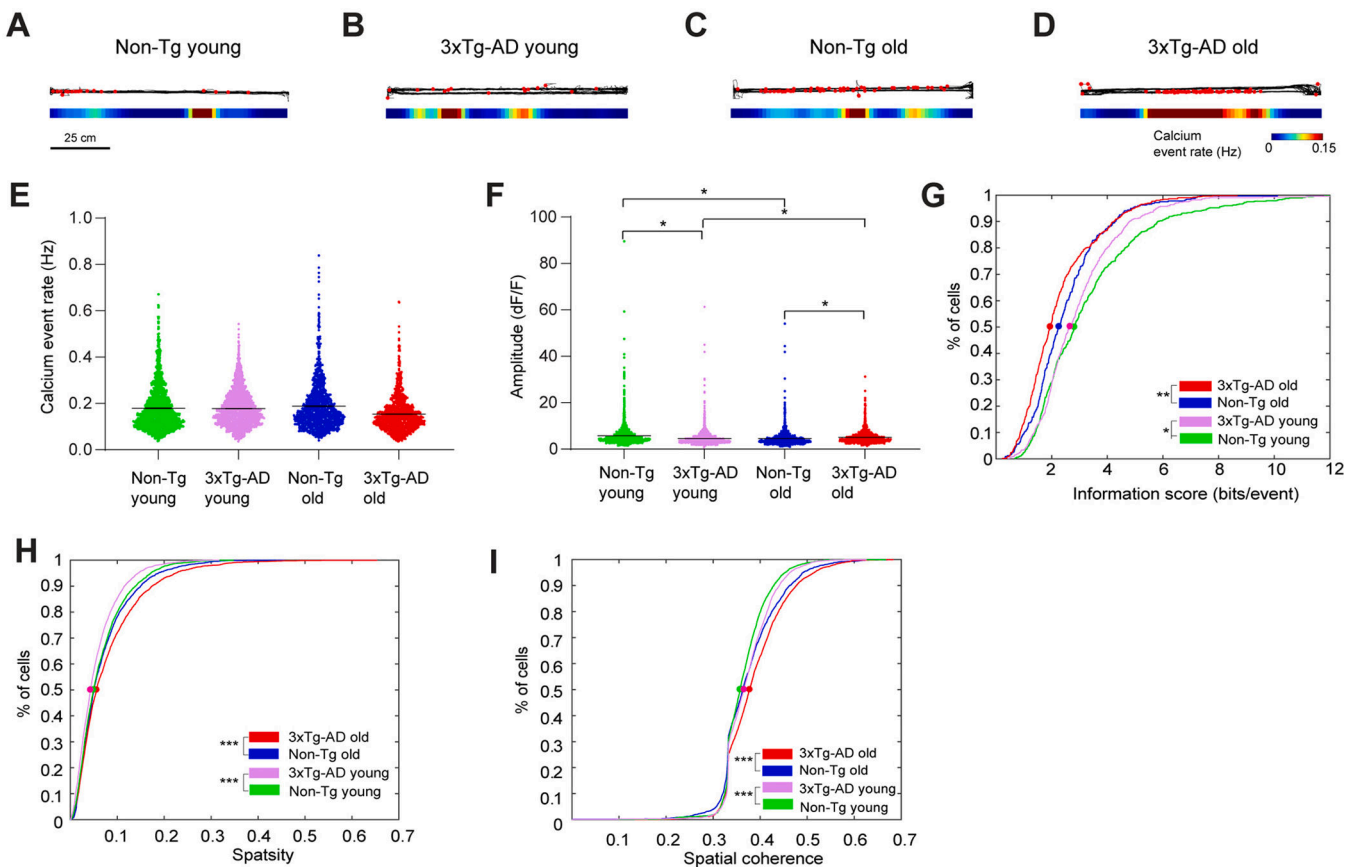
Fig. 4.
Linear track experiment data also support impaired spatial coding in 3xTg-AD hippocampal CA1. A-D. Example calcium event rate maps from mice running on a horizontal linear track with different genotypes and ages. Top: the black line represents the movement trajectory of mice. Superimposed red dots represent the locations where calcium events occur. Bottom: smoothed spatial rate maps. E. Violin plots of calcium event rates of all neurons from different groups of mice. Only the periods with movement speeds higher than 5 mm/s were used for event rate calculation, and event rates from trials with the same track direction were averaged. F. Violin plots of calcium event amplitudes of all neurons from different groups of mice. G. Cumulative distribution plots of spatial information scores (in bits/event) for all place cells from Non-Tg old, 3xTg-AD old, Non-Tg young and 3xTg-AD young mice, for both horizontal and vertical tracks in two directions. H and I. Cumulative distribution plots of sparsity (H) spatial coherence (I) values of all neurons for Non-Tg old, 3xTg-AD old, Non-Tg young and 3xTg-AD young mice, in both square and circle arena. LME analyses were used for E-F; two-sample Kolmogorov-Smirnov tests were used for G-I. *, ** and *** indicate the significance levels with the respective p values of <0.05, <0.005, and < 0.0005.
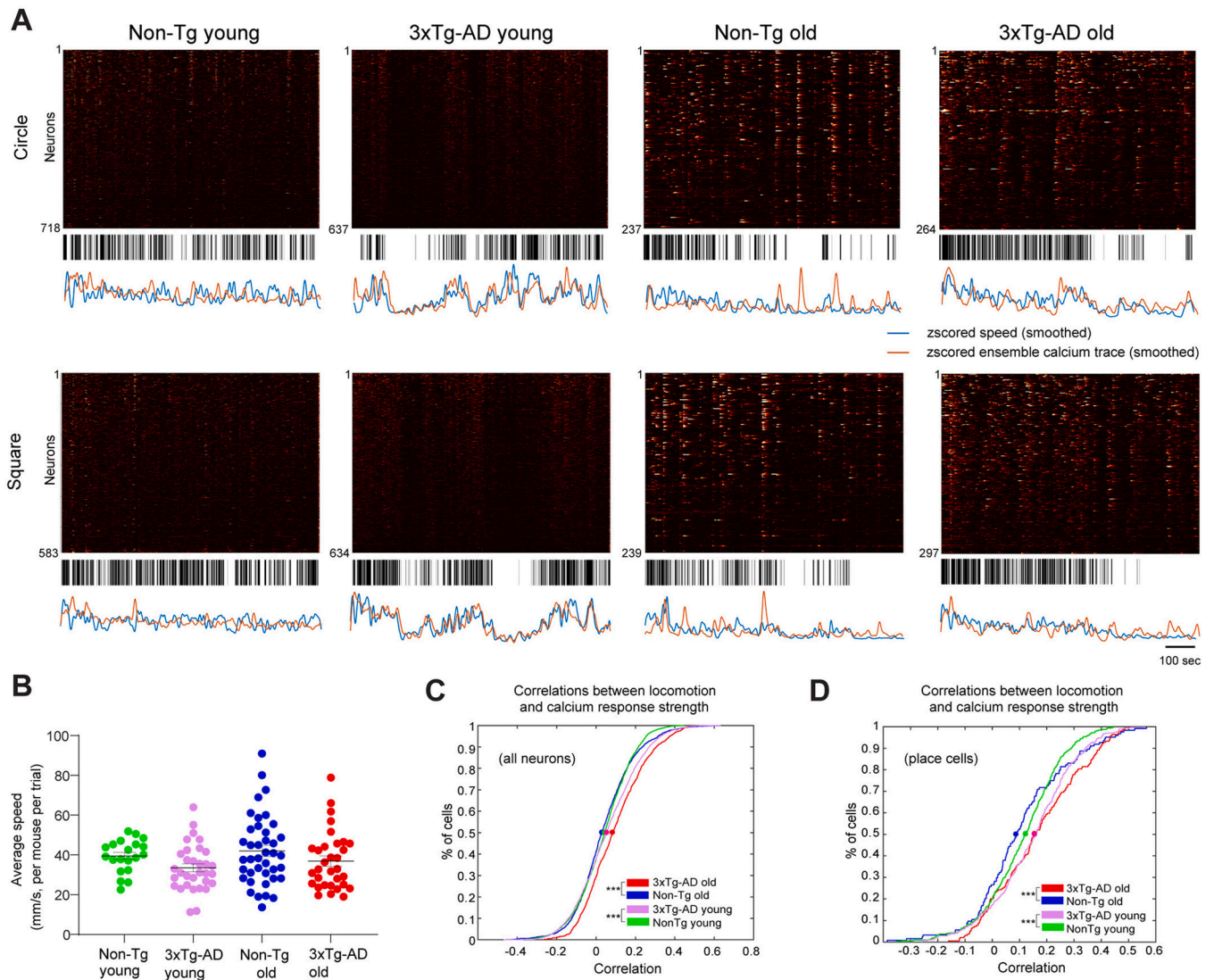
Fig. 5.

Neural calcium activities of 3xTg-AD mice exhibit stronger locomotion modulation than Non-Tg mice. A. Raster plots of calcium activities of hundreds of CA1 cells along with the time (top), movement epochs (middle) and comparison between the z-scored ensemble calcium signal trace and movement speed (bottom, ensemble calcium trace: orange; velocity trace: blue). The high-speed epoch is shown as the black bar at the time points where the movement speed is higher than the speed threshold, which is defined as the averaged median movement speed of the group. Four example sessions of Non-Tg young, 3xTg-AD young, Non-Tg old, and 3xTg-AD old mice, respectively, are shown. B. Distribution of mean movement speeds of different groups of mice. Each dot represents the mean speed of one mouse in one trial (circle or square). C. Cumulative distribution plots of correlation values between moving speed and all individual neuron's calcium response. Correlation values from trials with the same geometry are averaged. D. Cumulative distribution plots of correlation values between moving speed and all place cells' calcium trace. Two-sample

Kolmogorov-Smirnov tests were used for C-D. *, ** and *** indicate the significance levels with the respective p values of <0.05, <0.001, and < 0.0001.